


ORIGINAL ARTICLE

Open Access



Rapid early afterslip characteristics of the 2010 moment magnitude (Mw) 8.8 Maule earthquake determined with sub-daily GPS solutions

Kai Liu¹, Yangmao Wen^{2*} , Jing Zeng¹, Jianghui Geng¹, Zhao Li¹ and Caijun Xu²

Abstract

Ground surface deformations can be observed during the coseismic and postseismic periods. The accurate determination of displacements is of paramount importance for the assessment of the destructive power of large earthquakes and the characterization of fault behaviors. Therefore, we employ the sub-daily Global Positioning System (GPS) solutions at 19 GPS stations to determine the coseismic and postseismic deformations of the 2010 moment magnitude (Mw) 8.8 Maule earthquake. Using sub-daily GPS data, we can accurately measure both coseismic and early postseismic deformation signals, which can precisely identify the distribution of coseismic slip and the spatiotemporal evolution of early afterslip within the first 36 h. In particular, the sub-daily solution can provide more accurate and quicker results, nearly 10% smaller than those with the daily solution. Furthermore, there is significant ground motion in the immediate postseismic period, which decreases rapidly thereafter. The largest postseismic deformation observed during the first 2 h occurred at station CONZ and amounted to 3.6 cm. During the immediate postseismic period of the 2010 Maule earthquake, afterslip is the dominant mechanism, while poroelasticity plays a negligible role within the first 36 h. Meanwhile, early aftershocks tend to occur in the boundary and the inner part of the afterslip, indicating that the afterslip has the potential to drive the occurrence of aftershocks in the initial stages of postseismic activity.

Keywords 2010 Mw 8.8 Maule earthquake, Sub-daily GPS, Coseismic deformation, Early afterslip, Geodetic inversion

Introduction

The occurrence of earthquakes is accompanied by the accumulation and release of stresses within the Earth's crust (Burgmann & Dresen, 2008). When a large earthquake occurs, it not only releases a significant amount of stress, but also causes notable surface deformation (Perfettini & Avouac, 2004). By observing this deformation of

the ground surface, we can identify the activity characteristics and rupture scale of the seismogenic fault. Space geodetic techniques, such as the Global Navigation Satellite System (GNSS) and Interferometric Synthetic Aperture Radar (InSAR), can accurately measure the surface deformations in the vicinity of a seismogenic fault over a prolonged duration, encompassing pre-seismic, coseismic, and long-term postseismic deformations (Bilich et al., 2008; Bock & Melgar, 2016; Larson, 2009; Wright et al., 2004). A large earthquake is normally followed by noticeable postseismic deformations due to stress changes near the ruptured fault resulting from the release of the coseismic rupture (Perfettini & Avouac, 2004). Different mechanisms respond to this stress change in

*Correspondence:

Yangmao Wen
ymwen@sgg.whu.edu.cn

¹ GNSS Research Center, Hubei LuoJia Laboratory, Wuhan University, Wuhan, China

² School of Geodesy and Geomatics, Wuhan University, Wuhan, China



© The Author(s) 2024. **Open Access** This article is licensed under a Creative Commons Attribution 4.0 International License, which permits use, sharing, adaptation, distribution and reproduction in any medium or format, as long as you give appropriate credit to the original author(s) and the source, provide a link to the Creative Commons licence, and indicate if changes were made. The images or other third party material in this article are included in the article's Creative Commons licence, unless indicated otherwise in a credit line to the material. If material is not included in the article's Creative Commons licence and your intended use is not permitted by statutory regulation or exceeds the permitted use, you will need to obtain permission directly from the copyright holder. To view a copy of this licence, visit <http://creativecommons.org/licenses/by/4.0/>.

different ways, leading to the formation of distinct deformation patterns over various time scales (Freed, 2005). Previous studies focused on the mechanisms of deformation patterns involving the long-term deformation of the Earth's crust driven by various postseismic mechanisms, including afterslip, poroelasticity, and viscoelastic relaxation (Burgmann & Dresen, 2008). To observe postseismic deformation, we usually use the displacement time series provided by daily GNSS solutions, which are sufficient for long-term deformation observation (Bock & Melgar, 2016). Due to the limitations of conventional seismographs in detecting slow postseismic deformation signals, precise daily GNSS solution series have become a crucial data source for studying postseismic deformation features and investigating tectonic mechanisms.

However, significant postseismic deformation also occurs in the hours immediately following earthquakes, and such deformation signals cannot be captured by the daily GNSS solution series. Only a few studies focused on the unique early postseismic phase, mainly due to the limited availability of seismological (such as strong motion) and geodetic observations (such as GNSS and InSAR) to support such studies (Golriz et al., 2021; Tsang et al., 2019; Twardzik et al., 2019). The deformation induced by early afterslip may progress rapidly over a few hours, rather than days and weeks. These displacements can reach up to a few centimeters reported in several earthquakes (Langbein et al., 2006; Liu et al., 2022; Milliner et al., 2020; Perfettini & Ampuero, 2008; Tsang et al., 2019). There is limited knowledge about the characteristics of fault activity and its progression during the critical phase following an earthquake, especially in the first few hours. Early postseismic displacement observations can contribute to revealing the spatial and temporal evolution of afterslip on the fault plane. Analyzing the spatial relationship with the coseismic slip can better understand the activity characteristics of faults in their very early stages.

Subduction zones are the regions where one tectonic plate subducts under another, causing significant surface displacements and often resulting in the largest earthquakes in the world. On February 27, 2010, a powerful moment magnitude (Mw) 8.8 earthquake occurred on the coast of Maule, Chile (06:34:08, UTC). This earthquake ruptured more than 500 km along the boundary between the Nazca and South American plates. Before the 2010 earthquake, this area had three large historical megathrust earthquakes, the 1730 Mw 8.5–9.0 Great Valparaiso earthquake, the 1751 Mw 8.5 Concepción earthquake, and the 1835 Mw 8.5 earthquake (Vigny et al., 2011). Before the 2010 event, there were no major subduction earthquakes in the area since 1835, and this region was identified as a mature seismic gap (Ruegg

et al., 2009). Numerous studies investigated the coseismic rupture (Delouis et al., 2010; Tong et al., 2010; Vigny et al., 2011) and the afterslip based on geodetic and seismic observations (Aguirre et al., 2019; Bedford et al., 2013, 2016; Klein et al., 2016; Lin et al., 2013; Pena et al., 2019; Weiss et al., 2019), as well as analyzing the spatial and temporal distributions of aftershocks and finding a long-term correlation between afterslip distribution and aftershocks (Agurto et al., 2012; Lange et al., 2012; Rietbrock et al., 2012). However, most studies mainly focused on the long-term ground surface changes over long time scales (monthly or yearly), primarily using daily GNSS solution series and including the rapid early postseismic deformation in the coseismic estimate. In the immediate aftermath of the earthquake, typical daily solutions were insufficient in providing uninterrupted data on surface deformation within this timeframe. This limited our understanding of ground displacement and fault activity during this early period. To tackle this issue, we can concentrate on the early post-seismic period and investigate the characteristics in the evolution of afterslip and aftershocks during the first few hours since rupture completed by sub-daily GNSS solutions, in contrast to previous long-term research.

To assess the near-field deformation induced by the 2010 Mw 8.8 Maule earthquake and to study the coseismic rupture, as well as the temporal and spatial characteristics of the post-earthquake rupture, we collected the observations at 19 continuously operating Global Positioning System (GPS) stations in the vicinity of the epicenter. The distribution of GPS stations is shown in Fig. 1. We acquired the GPS solution series of each station with sub-daily resolution and computed the post-seismic displacements resulting from the mainshock. Then, we compared the discrepancies in coseismic deformations obtained at different temporal resolutions. Based on them, we further examined the spatial and temporal properties of the early afterslip development, as well as its association with the distribution pattern of aftershocks. We attempted to reveal the activity characteristics and potential driving mechanism of faults after the rupture of a large earthquake during the very early period.

Data processing and inversion model

GPS processing

We collected the observations at 19 continuously operating GNSS stations with a sampling interval of 30 s, which can be downloaded from the Chilean Seismological Center (CSN, <http://gps.csn.uchile.cl/data/>). We obtained the sub-daily GPS solution series for each station using software PRIDE PPP-AR (Geng et al., 2019). The kinematic GPS processing strategies differ from static solutions. For each station, kinematic positions are calculated

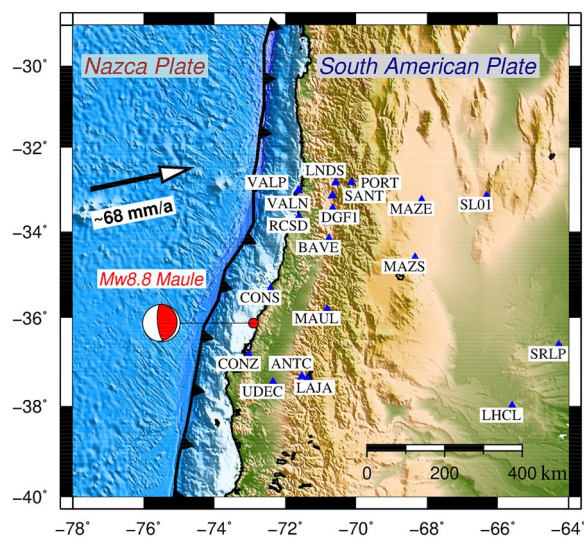


Fig. 1 Distribution of Chilean GPS network around the area of the 2010 Maule earthquake. The red dot shows the epicenter of the 2010 Mw 8.8 Maule earthquake from (United States Geological Survey, USGS). The blue triangles represent GPS sites. The black triangular lines indicate the boundary between the Nazca plate and the South American plate, where the Nazca plate subducts beneath the South American plate at a rate of ~ 68 mm/a (Altamimi et al., 2007). The location of the mainshock is represented by the red dots, and the beach ball indicates that this is a megathrust earthquake

using the precise point positioning technique for a period of 5 days (2 days before and 2 days after the earthquake), as shown in Fig. 2 and Figure S1. The undifferenced ambiguities are resolved to obtain accurate results. The influences of solid earth tides and ocean loading were removed from the positions. To be more specific, precise satellite orbit, clock, and phase bias rapid products from the third International GNSS Service (IGS) reprocessing campaign were used in the data processing; positions and receiver clocks were both treated as white-noise-like parameters; ionosphere-free observations were used to eliminate the influence of first-order ionospheric delays while troposphere delay was estimated as random-walk parameters. Second-order ionosphere delay was corrected by using the Global Ionosphere Map (GIM) product of the Center for Orbit Determination in Europe (CODE). The multipath error was ignored in the data processing. The effect of higher-order ionospheric delays is essentially in the order of millimeters in kinematic processing and can therefore be ignored. (Banville et al., 2017). For each station, we calculated the linear trend of the GNSS solution sequence over a short period based on the pre-seismic sequence over 50 h before the earthquake. This processing strategy is consistent with the method of Twardzik et al. (2019). After obtaining the linear trend, the entire position time series was corrected to

obtain a position series that is only affected by postseismic deformations. The seasonal amplitude was ignored since it was found to produce negligible changes within such a short period. Subsequently, we further performed sidereal filtering based on the GPS observations of the previous 2 days (Geng et al., 2018; Genrich and Bock, 1992).

Inversion model

We performed an inversion of the coseismic slip and afterslip distribution based on the coseismic deformations of 19 GNSS stations. The fault was constructed according to the Slab 2.0 model (Hayes et al., 2018), which consists of 555 rectangular 20×20 km patches with a length of 740 km along strike and a width of 300 km along dip, due to the large magnitude of the earthquake and the large rupture extent. The inversion was then performed using the software SDM (Wang et al., 2011) with a homogeneous elastic half-space model (Okada, 1992) to calculate the displacement of each GPS station due to slip on each patch. Figure 3(a) illustrates the degree of agreement between our model and the model Slab 2.0. The two models overlap almost completely in the three profiles from north to south, particularly in the area below 60 km depth, suggesting that the fault structure we have constructed is reliable. To assess the resolution of our model, we performed a checkerboard test. We divided the fault plane into 18 sub-patches, each with a size of 100 km wide and 120 km long, set to the presence (1 m) or absence (0 m) of slip. Then, based on the input slip distribution (Fig. 3b), the displacement of each GPS station can be obtained with a homogeneous elastic half-space model. By using these displacements as input parameters, the output slip distribution can be inverted (Fig. 3c) and compared with the input slip distribution. The checkerboard test revealed that the overall resolution of the model is good in the central and northern regions have higher resolution, but the southern region has poor resolution because there are no GNSS stations.

Results

After obtaining the GPS solution series, we further calculated the coseismic and postseismic displacements. To ensure efficient and uniform calculation of coseismic displacements for each GPS site, we utilized the 10 min postseismic mark as the computation node. This time window is sufficient for the completion of seismic wave propagation from the network, thus circumventing dynamic seismic wave effects from biasing the displacement calculation (Figure S2). The time series occurring 10 min after the onset of the earthquake is regarded as the postseismic phase in the computational sense, not in the physical definition. The postseismic sequence was fitted

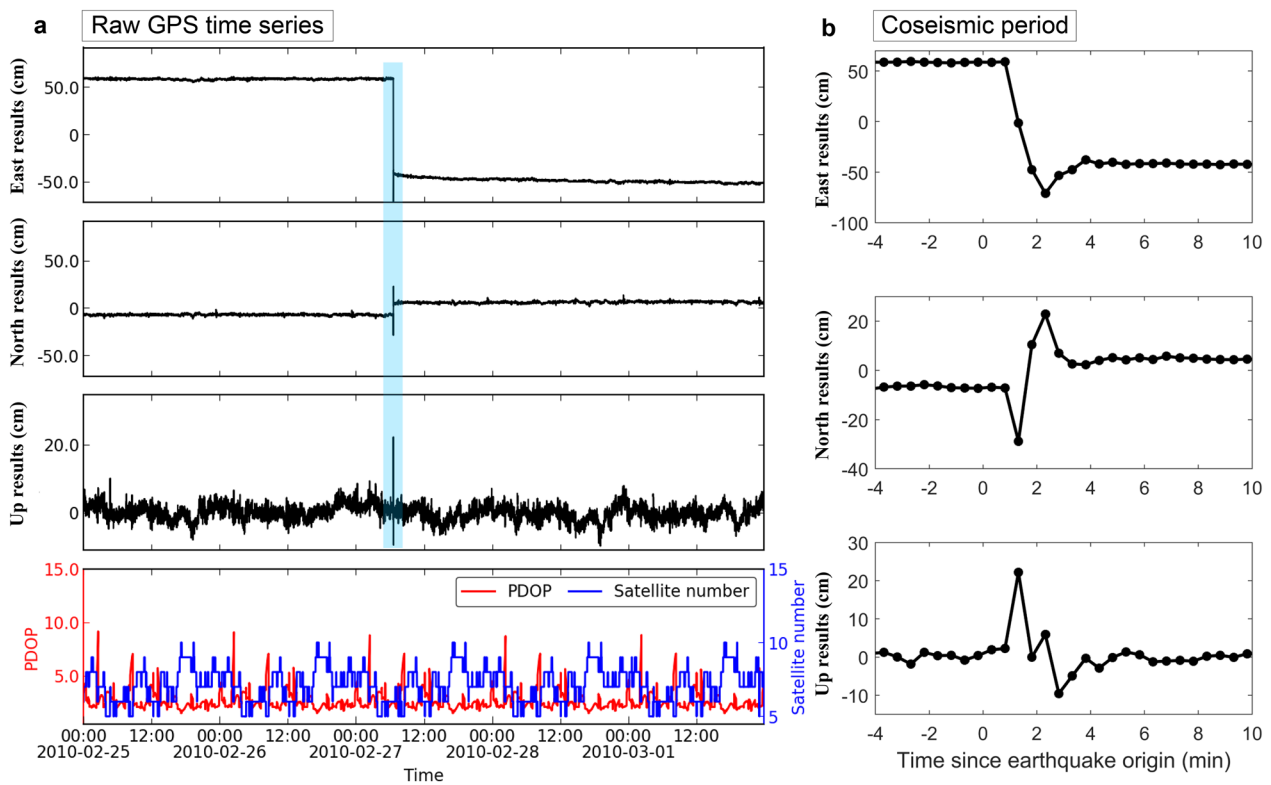


Fig. 2 GPS solution series of station MAUL calculated with software PRIDE PPP-AR. Panel **a** shows the east, north, and vertical displacement components, position dilution of precision (PDOP), and number of visible satellites. Panel **b** show the coseismic displacement during the rupture period highlighted in panel **a**

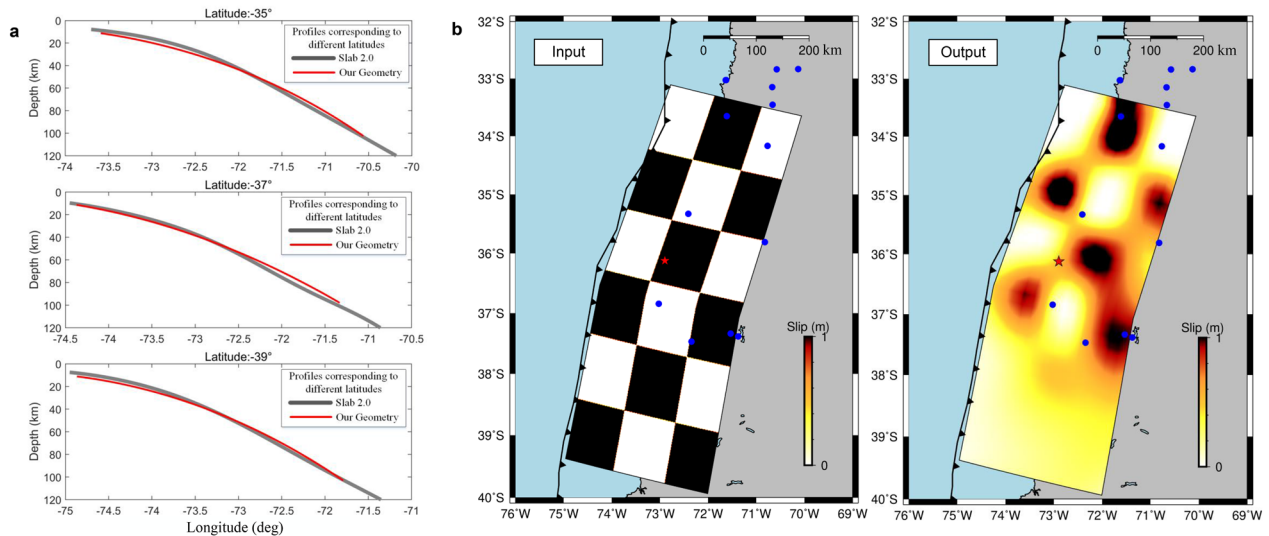


Fig. 3 Fault geometry (a) and checkerboard test (b) of our model. In panel **a**, the profiles along latitude lines -35° , -37° and -39° are shown from top to bottom, where the gray line represents the SLAB 2.0 model, and the red line represents our fault model. Panel **b** shows the input and output results of the checkerboard test. Each patch is set to a size of 100×120 km with black representing 1 m of slipping and white being no slipping

using the power function model (Liu et al., 2022) to derive a smooth postseismic time series, with the deformation data obtained per station every 2 h for 36 h following the earthquake with uniform sampling (Figure S3). We employed the mean value of the GPS solution series from 10 min before the earthquake as the initial value for the pre-seismic sequence. Following this, we combined the postseismic segment positions and sequentially computed the coseismic and postseismic displacements.

Coseismic and early postseismic displacements obtained by sub-daily solutions

Coseismic displacements are a crucial source of data for assessing earthquake damage and analyzing deformation mechanisms. However, traditional daily solutions typically calculate the coseismic displacements using the average of the days before and after the earthquake, resulting in a gap of over 48 h between the two calculation nodes. This can lead to the early postseismic component being inaccurately included in the coseismic displacement, resulting in overestimation. To distinguish precisely between the coseismic and postseismic phases, and obtain accurate coseismic displacements, it is imperative to determine these phases via displacement sequences with high temporal resolution as swiftly as feasible (Golriz et al., 2021).

To evaluate the difference between the daily and sub-daily solutions in the coseismic displacements, we calculated sub-daily and daily coseismic displacements based on the position of 10 min and 24 h after the earthquake, respectively. Table 1 shows the coseismic displacement values for both solutions and the differences introduced by the undefined early postseismic displacement. The coseismic deformation is mainly concentrated in the eastward component, and the largest deformation occurs at the station CONS, which is close to 4.7 m. The deformations of 8 out of 19 GPS stations exceed 0.5 m, and 5 exceed 1 m. The differences between the two approaches are a few centimeters in magnitude with the most notable variances occurring in the eastern component, in line with the deformation tendencies of megathrust earthquakes. The largest biases occur at station CONZ and reach almost 10 cm. The differences in the eastern components are significantly larger, representing the fact that fault slip activity continued and was more active during the first 24 h after the earthquake, producing significant postseismic surface deformation. It is statistically demonstrated that the daily solution overestimates the coseismic displacements by nearly 10% in comparison to the sub-daily solution, which aligns with earlier research (Tsang et al., 2019; Twardzik et al., 2019).

From the distribution of ground surface displacements (Fig. 4), the major displacements of this earthquake are

Table 1 Coseismic displacements of the 2010 Mw 8.8 Maule earthquake calculated by daily solution (after 24 h) and sub-daily GPS (after 10 min), and their differences

Station	Daily results in different directions (cm)			Sub-daily results in different directions (cm)			Biases in different directions (cm)		
	East	North	Up	East	North	Up	East	North	Up
ANTC	-78.21	17.51	-3.92	-72.77	16.75	-3.52	-5.44	0.76	-0.40
BAVE	-115.38	-19.29	-9.21	-109.02	-18.89	-8.08	-6.36	-0.40	-1.13
CONS	-470.31	-39.08	-39.69	-466.00	-36.12	-36.36	-4.31	-2.96	-3.33
CONZ	-298.71	-72.37	-1.73	-288.77	-72.37	-2.02	-9.93	0.00	0.28
DGF1	-44.05	-19.12	-1.64	-40.98	-18.87	-2.59	-3.07	-0.25	0.95
LAJA	-69.66	17.36	-1.32	-63.24	16.16	1.52	-6.42	1.20	-2.84
LHCL	-6.51	1.92	1.00	-5.82	1.46	1.01	-0.69	0.46	-0.01
LNDS	-14.87	-9.06	-1.43	-12.12	-8.90	-0.66	-2.75	-0.16	-0.77
MAUL	-107.09	12.99	-0.89	-100.70	11.87	-0.07	-6.39	1.11	-0.83
MZAE	-9.40	-4.56	4.85	-9.52	-3.58	5.44	0.12	-0.98	-0.59
MZAS	-19.44	-0.35	0.98	-19.34	-0.16	2.05	-0.10	-0.18	-1.06
PORT	-13.93	-8.62	0.56	-12.64	-7.92	0.82	-1.29	-0.70	-0.33
RCSD	-73.06	-34.44	-17.57	-67.14	-34.55	-17.40	-5.91	0.11	-0.17
SANT	-25.89	-14.54	-3.34	-24.94	-14.06	-2.76	-0.95	-0.49	-0.57
SL01	-6.92	-2.29	-0.50	-6.92	-2.29	-0.47	0.00	0.00	-0.03
SRLP	-5.81	1.12	2.60	-5.50	1.09	2.59	-0.31	0.03	0.01
UDEC	-149.11	16.00	-36.46	-140.92	16.00	-36.47	-8.18	0.00	0.01
VALN	-11.04	-2.69	-3.76	-8.36	-2.13	-3.56	-2.68	-0.55	-0.19
VALP	-7.44	-1.17	-13.52	-5.79	-1.19	-13.75	-1.64	0.02	0.23

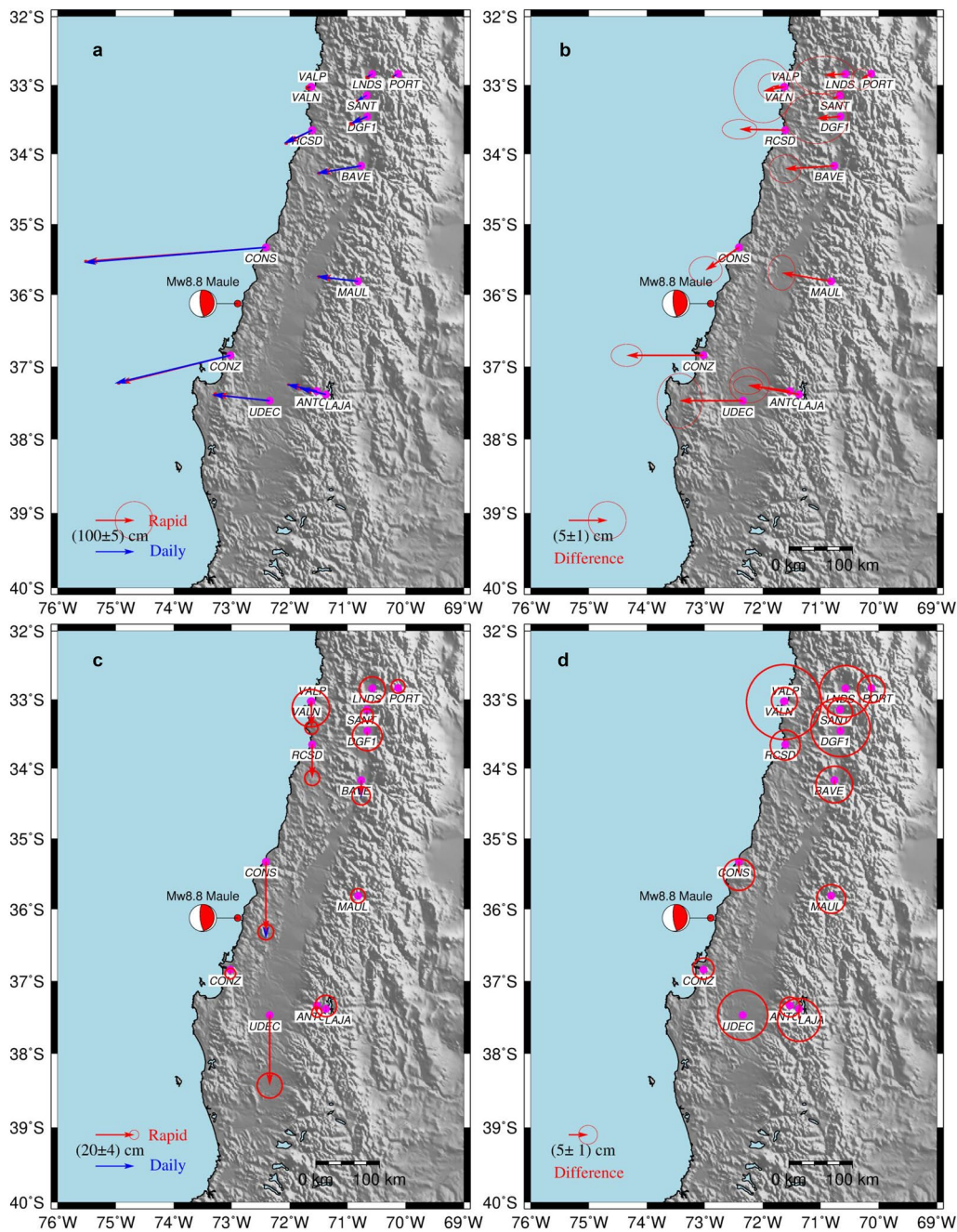


Fig. 4 a Horizontal and c vertical components of coseismic displacement calculated by rapid (10 min) and daily (24 h) solution, and their difference for b horizontal and d vertical components. The red and blue arrows indicate sub-daily (rapid) and daily solutions, respectively

concentrated in the area near the epicenter and close to the coast. The directions of horizontal displacements of nearby stations CONS and CONZ display some variability, indicating that the earthquake’s rupture pattern is relatively complex. The differences between the coseismic displacements calculated at different resolutions in the horizontal and vertical directions are mainly

concentrated in the region of larger deformations, which is in the range of 35°–38°S. Only two stations, CONS and LAJA, exhibit differences close to 4 cm in the vertical component, while all other stations show vertical differences less than 2 cm.

After calculating the coseismic displacements with kinematic GPS, we further analyzed the surface

deformations in the very early postseismic period. Figure 5 shows the postseismic deformations in a sampling interval of 2 h. The postseismic deformation is extremely significant in the eastern direction, which is much larger than that in the northern and vertical directions (Figure S3 and Figure S4). Within the initial 2 h, several stations had more than 2 cm in the cumulative deformation of the eastern component, with CONS recording 3.6 cm. The postseismic displacement decayed very quickly, and in the first 6 h, the cumulative deformation of the East, North, and Up components reached 78%, 76%, and 74% of the cumulative deformation in the first 12 h, respectively, which is more than half of the cumulative displacement in the first 36 h. The above findings suggest that during the initial postseismic phase, deformation rate is high and represents the most active period of the entire postseismic phase. As such, recording surface

deformation during this time is crucial for comprehending early fault activity.

Rapid coseismic slip distribution

Postseismic ground deformation undergoes a gradual decay process evident in long-term postseismic GNSS solution series. However, our ability to present the surface deformation in the initial few hours after the cessation of earthquake rupture using daily GNSS solutions is restricted due to inadequate temporal resolution. We captured this continuous ground deformation signal from the kinematic GPS solution series to further identify the surface displacement information since the rupture was completed. Based on the two coseismic displacement calculations, we further performed an inversion of the coseismic slip distribution of different time scales (Fig. 6).

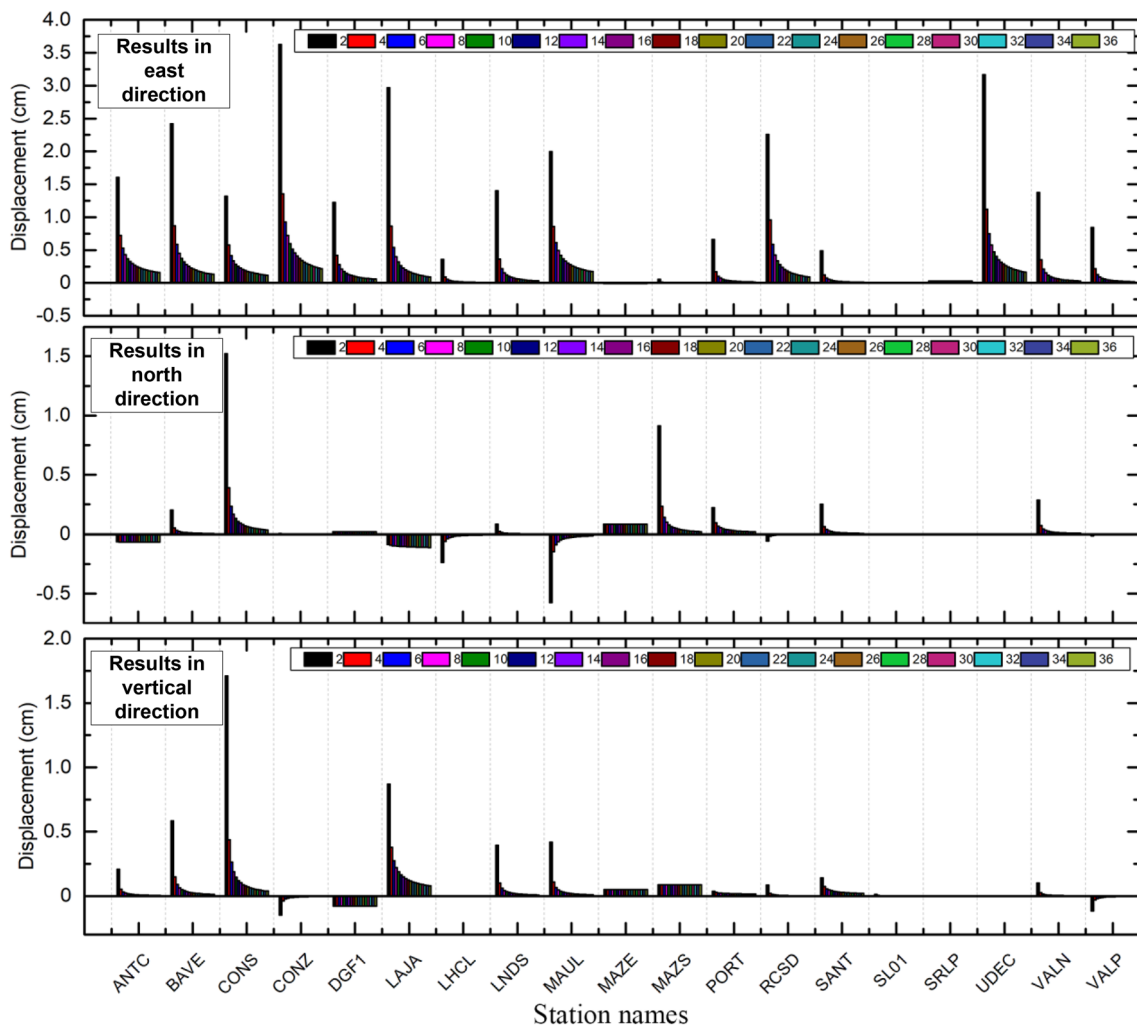


Fig. 5 Very early postseismic displacement was captured by kinematic GPS during the first 36 h since the earthquake ruptured. Each column represents the cumulative displacement of 2 h at different components

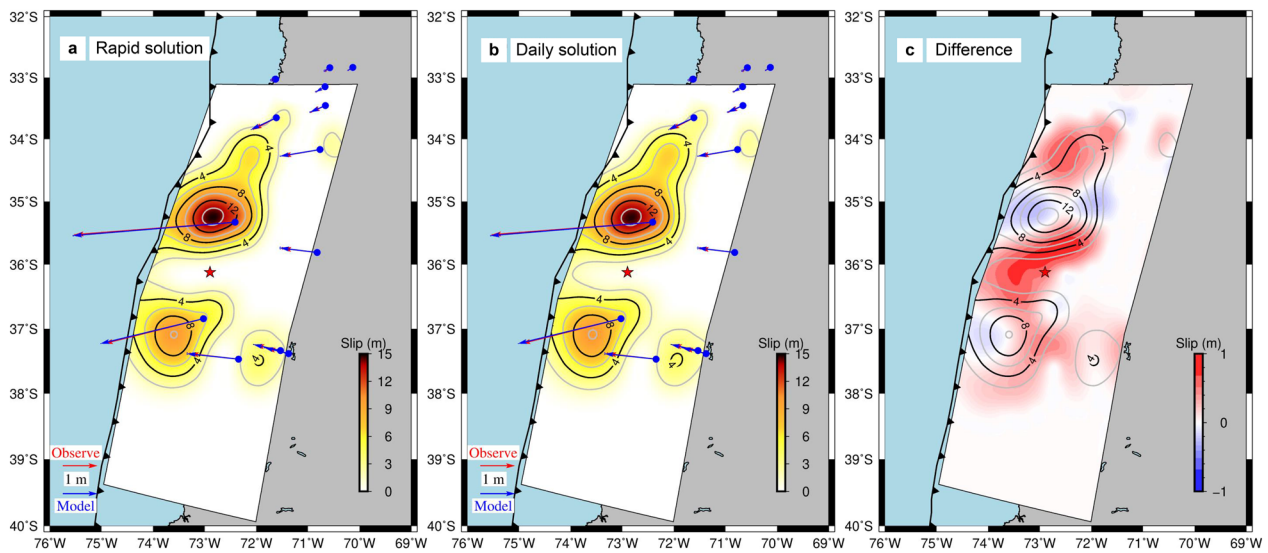


Fig. 6 Slip distribution inverted by **a** rapid and **b** daily GPS solution, and **c** difference between the two solutions. The red star represents the location of the epicenter, and the black and gray contours show the main areas of coseismic slip

The major ruptures of the 2010 Maule earthquake were concentrated in two areas, north and south of the epicenter. The maximum slip occurs in the slip zone near 35°S, reaching 14.6 m. This area is the main slip zone of this earthquake and ruptures northward with the strike. The concentrated slip zone south of the epicenter is near 37°S, with a maximum slip of more than 10 m. A smaller slip zone also occurs in the downdip area with a slip of roughly 4 m. The rapid coseismic slip distribution shows that the earthquake's coseismic rupture has an average slip of 1.96 m, with an average rake angle of 111.4°, and releases a seismic moment of $1.17 \times 10^{22} \text{ N} \cdot \text{m}$, which corresponds to a moment magnitude of about Mw 8.68. The distribution of the daily-solution coseismic slip (Fig. 6b) is basically the same as that of the rapid coseismic slip spatially, with a maximum slip of 14.6 m, an average slip of 2.06 m, an average rake angle of 111.7°, and the released seismic moment is $1.21 \times 10^{22} \text{ N} \cdot \text{m}$, which is about 4% larger than that of the fast coseismic slip distribution, corresponding to the moment magnitude of Mw 8.69. The difference in the released energy between the two distributions is $4.13 \times 10^{20} \text{ N} \cdot \text{m}$, which is equivalent to a Mw 7.7 earthquake.

The differences between the two coseismic slip distributions are shown in Fig. 6. It is evident that in the following 24 h, the slip amounts in most regions of the coseismic slip distributions have risen slightly in comparison to the rapid coseismic slip distribution. The increase in slip amount is mainly concentrated near the epicenter, with a maximum difference of 0.85 m, while a negative situation occurs in the region of maximum mainshock rupture, located around the 35°S line. Further to the

north is an area with smaller increments of slip. Generally, these increments occur mostly in the edges of the 4-m contours of the rupture zone caused by the mainshock and are connected to each other. Although these variations have very little impact on coseismic ruptures, and the slip measured at different points in time is almost the same, the distribution of this magnitude of slip is extremely important for postseismic afterslip and may be driven by early afterslip. Therefore, it is crucial to make an accurate distinction between coseismic and postseismic displacements.

Evolution of afterslip in the early stage

Following the completion of the rupture, afterslip took place swiftly on the fault plane within the initial 36 h (as shown in Fig. 7 and Figure S5). During the first 2 h, after slip occurred in the boundary of the mainshock rupture area with some overlap, and no afterslip occurred in the core region of the coseismic rupture. Afterslip developed two small slip zones: one adjacent to the epicenter and at the periphery of the 4 m contour of the coseismic slip, and the other in the northern area of the major coseismic slip. Generally, most of the slip zones are in the central and shallow regions of the fault, especially in the gap between the two main slip zones formed by the coseismic slip. The afterslip illustrated a remarkable spatial expansion between 4–12 h. The two initial zones of afterslip concentration, which emerged during the first 2 h, progressively increased in size over time. The afterslip zone to the north almost entirely overlapped with the minor branch extending from the coseismic slip. Meanwhile, the afterslip zone near the epicenter gradually filled the gap

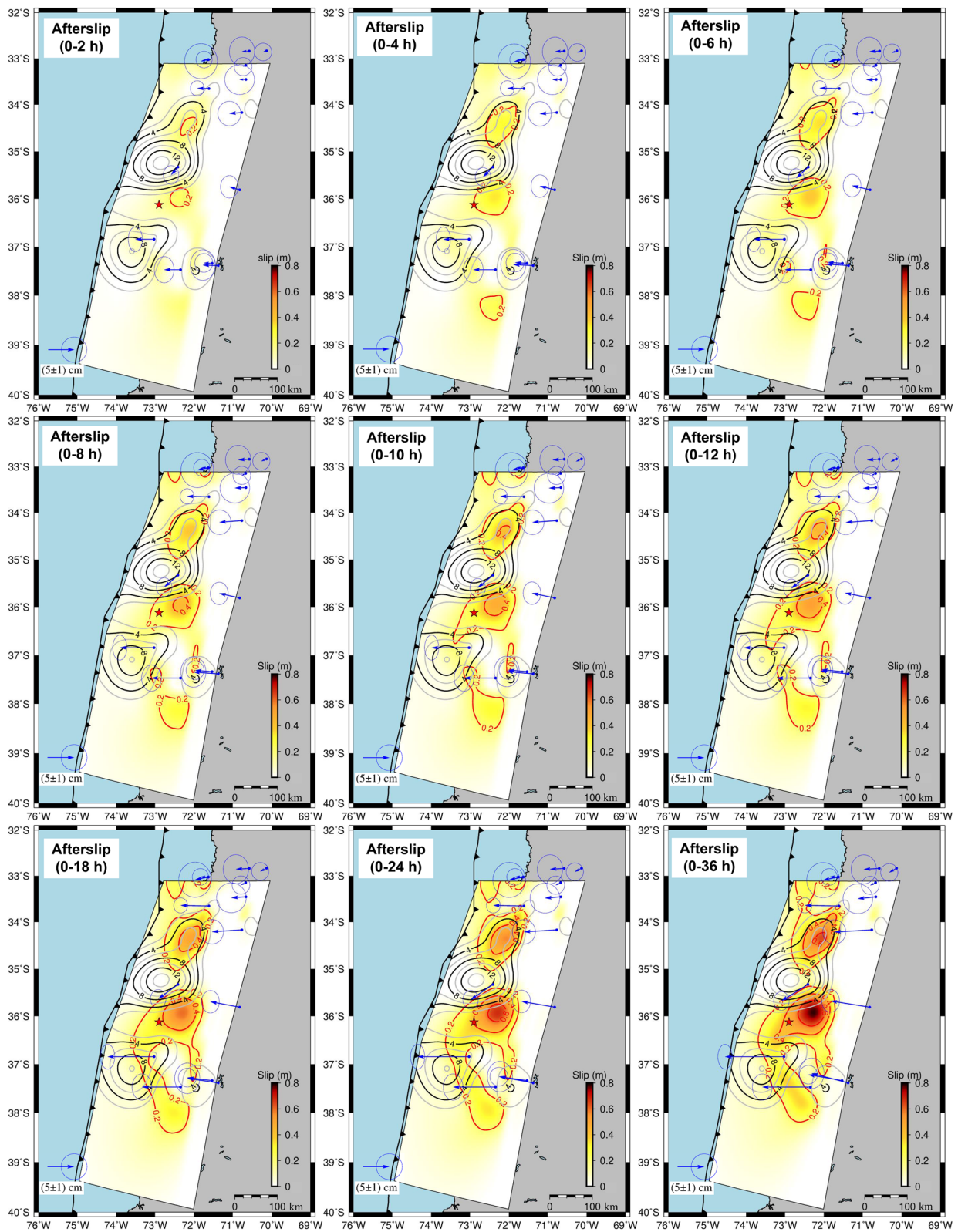


Fig. 7 Evolution of early afterslip during the first 36 h since earthquake rupture finished. Black and gray contours show the distribution of coseismic slip, and the red contours present the afterslip distribution. Blue vectors indicate the GPS displacement field with a 95% confidence interval

in the middle of the two concentration zones of coseismic slip. In the southern region of the deeper part of the fault, a concentration zone of slip activity emerged, located in the southern part of the smaller slip zone in the deeper part of the syncline and gradually extending towards the shallow part and the epicentral direction of the earthquake. During the period of 12–36 h, the concentration zone of the afterslip remained stable. The main features of the afterslip included the gradual consolidation of the scattered slip zones and a gradual increase in the amount of slip. Over the same time frame, the concentration zone of the afterslip remained stable with no tendency of expanding outwards, and the main characteristics were the gradual merging of the dispersed slip zones and the gradual increase in the amount of slip. The slip zones within the fault are merged in the central and southern regions, which occurs in 12–18 h near 37°S. Combined with the variation of seismic moments within the different periods (Figure S6), it can be found that the very early postseismic energy release is also characterized by a rapid decay. Therefore, the afterslip evolution process in the very early postseismic period can be divided into two phases, an expansion period of 0–12 h, and a stabilization period of 12–36 h.

A clear similarity can be observed between the difference in coseismic slip (Fig. 6c) and the postseismic slip distributions (Fig. 7). The core area of the postseismic slip distribution almost coincides with the difference of the two coseismic slip distributions. This suggests that the very early postseismic slip is absorbed into the coseismic slip distribution calculated based on the daily solution. Considering the smoothing process during the inversion, despite the high similarity between the two distributions, they are not equivalent. Therefore, carrying out independent postseismic inversion is necessary to analyze the variability of the coseismic displacements between the daily and sub-daily solutions. As a result, the daily GPS solution consistently overestimates the release of energy during the coseismic phase and the activity of the fault, which is consistent with previous studies (Golriz et al., 2021). Furthermore, if the observed displacements in the very early postseismic period are ignored, the fault evolution process in the postseismic phase, as revealed by the daily GPS solution series, will be incomplete. Consideration of the attenuation properties of postseismic deformation is crucial for a comprehensive study of postseismic physical mechanisms, particularly at the onset of the postseismic phase.

Discussion

Assessment of seismic displacement monitoring accuracy

Accurate displacement observation is important for the monitoring and inversion of earthquakes. Measurement

accuracy is an important assessment indicator to ensure the validity of inversion results. In the Maule earthquake, the accuracy of deformation observed with GPS was basically maintained at the centimeter level (refer to Table S1-S4). The accuracies of coseismic and postseismic displacements calculated in the east, north, and vertical directions are comparable, where the uncertainties are within 1 cm in the horizontal direction and approximately 2 cm in the vertical direction.

Most of the coseismic displacements are much larger than their measurement errors. The vast majority of coseismic displacements are in the order of decimeters or more. These deformations can be identified by the displacement waveforms in the coseismic phase (see Figure S2). Therefore, the coseismic observations can provide reliable information for the inversion of the coseismic slip distribution. The postseismic eastward displacements exceeded 2 cm, which is much higher than the measurement uncertainty. The northward and vertical displacements are mostly less than 1 cm and insignificant compared to the measurement noise. In terms of the reliability of calculated seismic displacement, the postseismic displacement is much smaller than the coseismic displacement. The inversion of postseismic slip distribution is dominated by the eastern component of deformation, as the deformations in the northward and vertical directions are small. The eastward deformation is significantly larger than the measurement error, indicating the inversion results are accurate and reliable.

Although the measurement noise of the sub-daily solution is significantly larger than that of the daily solution, the amplitude of the significant early postseismic deformation signal in the 2010 Maule earthquake largely exceeds the measurement uncertainty of the sub-daily GPS solution. This suggests that sub-daily GNSS solution can compensate for the lack of temporal resolution of the daily solution and play a greater role in the coseismic and early postseismic displacement monitoring of large earthquakes.

Role of poroelasticity during the very early period

Postseismic displacement is controlled by a variety of driving mechanisms, including afterslip, and poroelastic and viscoelastic relaxation (Wang et al., 2012). These mechanisms react to stress changes that occur in different timescales due to coseismic rupture, fault geometry, and lithospheric rheology. Generally, the deformation caused by poroelastic relaxation is in the near-field region of the seismogenic fault and occurs approximately in the early postseismic period, from days to months after the earthquake (Jonsson et al., 2003). Considering the surface deformation produced by poroelasticity, the elastic problem is typically solved with undrained and drained elastic

parameters to find the instantaneous and fully-drained deformation states (Peltzer et al., 1996). The difference between them is taken as the total poroelastic deformation (McCormack et al., 2020).

Based on the coseismic rupture model, we assessed the potential contributions resulting from poroelastic rebound by comparing the models of coseismic displacements under drained and undrained conditions. We assumed Poisson’s ratios of 0.25 and 0.27 for drained and undrained conditions, respectively. By altering the Poisson’s ratios, we can evaluate the surface deformation caused by fluid flow resulting from the changes in pore pressure. Figure 8 illustrates the poroelastic effects on the deformation during the 2010 Maule earthquake. The predicted deformation is concentrated in the near-field, while the deformation in the far-field is almost negligible. All the deformations are in the millimeter scale, except for CONS, CONZ, and UDEC, where the vertical variation exceeds 1 cm. The coseismic deformations at these three stations are also among the largest, indicating that the poroelasticity-induced deformations are correlated with coseismic deformations (Table S5). The postseismic deformations observed are significantly greater than the potential poroelastic deformations simulated, particularly in the eastern component.

Figure 8 shows the total poroelastic deformation, which is the cumulative deformation of months after the mainshock, rather than in the early postseismic period (several hours). Considering the very early postseismic time scale, the poroelastic deformation within this period will be a smaller part of the total value. Therefore, the contribution of the poroelastic rebound mechanism to the postseismic deformations during the very early period is relatively weak. Simultaneously, the potential deformation caused by poroelasticity is a gradual accumulation process. Therefore, it may be necessary to combine it with long-term observations to better evaluate its spatial and temporal properties (Pena et al., 2022). Our result indicates that the effects of poroelasticity cannot directly contribute to the significant displacement during the first few hours, which suggests that the dominant mechanism causing significant near-field surface deformation in the very early postseismic period of the 2010 Maule earthquake is the afterslip.

Relationship between afterslip and aftershocks

After an earthquake, afterslip and aftershocks are two interrelated processes that frequently transpire. Their simultaneous occurrence can exacerbate the destruction caused by the mainshock. While the connection between

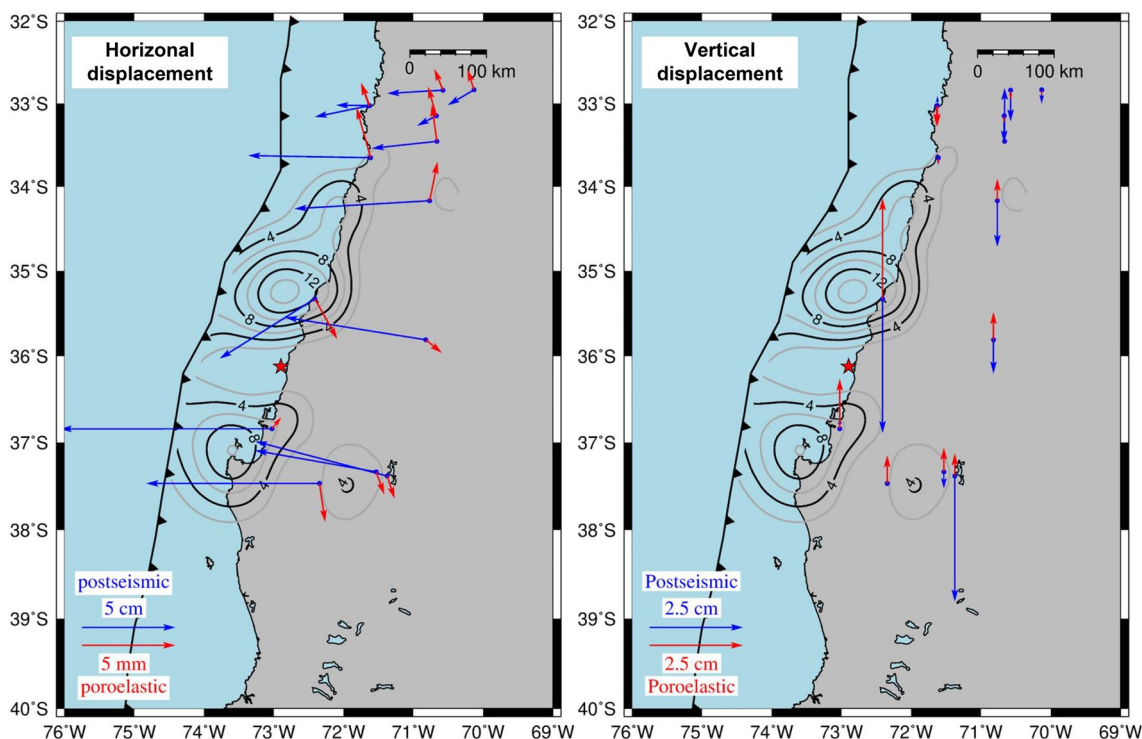


Fig. 8 Comparison of measured displacements (blue vectors) during the first 36 h and total poroelastic deformation (red vectors) following the earthquake. Black and gray contours represent the main coseismic slip distribution. The red star represents the location of the epicenter

afterslip and aftershocks remains a topic of debate, the findings indicate that afterslip may affect the development of aftershocks (Agurto et al., 2012; Lin et al., 2013; Rietbrock et al., 2012). Therefore, additional research is necessary to comprehend the mechanism of this phenomenon, including whether afterslip plays a role in the occurrence of aftershocks, and whether there is a correlation between the locations of aftershocks and the distribution of afterslip during the very early postseismic period.

We collected a catalog of all aftershocks greater than magnitude 2.5 within 36 h of the Maule earthquake from the USGS (<https://earthquake.usgs.gov/earthquakes>). Further, we investigated the spatial correlation between aftershocks and afterslip by counting the number of aftershocks within 0.25° of an aftershock and combining this with the spatial distribution of afterslip (Fig. 9). Within 36 h of the earthquake, there were 502 aftershocks distributed across the rupture area, with the majority occurring inside, and very few aftershocks outside the fault plane. Most of the aftershocks are in the central and shallow parts of the fault, forming four aftershock concentration zones (green circles in Fig. 9). The correlation between the distributions of aftershocks and coseismic slip is insignificant. Although the aftershocks cover the two primary rupture regions of the coseismic event, their distribution lacks any clear overlap or complementary spatial relationship. Comparing the distribution with that of the afterslip, we discovered that the aftershock and afterslip concentration areas coincide primarily in the north part of the fault, especially in the region around 34°S , where the local maximum of the afterslip is the aftershock concentration area. In the central part of the fault, from 34.5°S to 37°S , the aftershocks are predominantly distributed in the edge of the afterslip, coinciding with the 0.2 m contour, and are in the shallow region. On the fault's southernmost side, there is a slight deviation with the aftershocks in the edge of the afterslip. There is a noticeable difference between the two, with the aftershocks mainly concentrated in the shallow part near the 0.1 m afterslip contour, while the main body of the afterslip progresses towards the deeper part of the fault and no aftershocks occur at the location with the greatest amount of local slip. Considering the absence of GPS stations in the southern region and the weakness of the model's resolution in the south (shown in Fig. 3), the reliability of the slip in this region is relatively poor compared to the central and northern parts of the fault plane.

To investigate the correlation between the timing and locations of aftershocks and afterslip, we divided the first 12 h into six 2-h intervals and three longer periods of 12–18, 18–24, and 24–36 h (Fig. 10). During the 0–2-h period, aftershocks are distributed relatively evenly with a small area of aggregation. The dot color indicates that

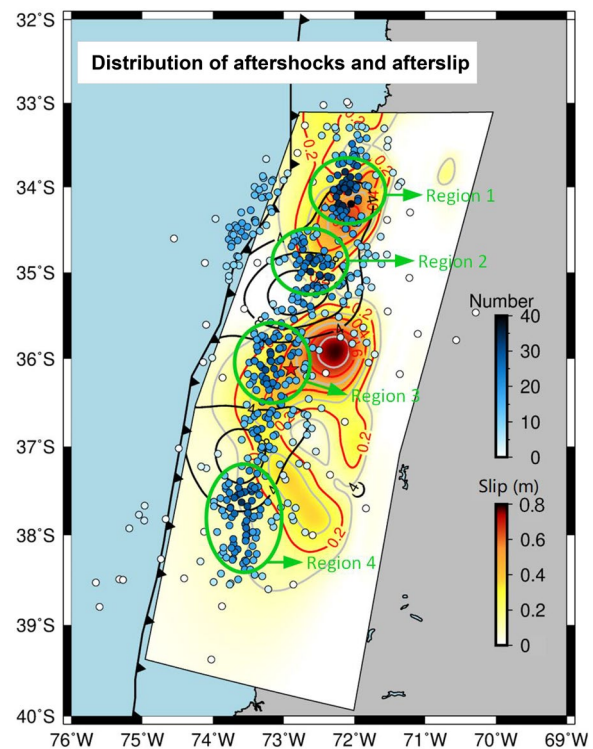


Fig. 9 Distribution of aftershocks and afterslip during the first 36 h after the 2010 Mw 8.8 Maule earthquake. The dots represent the locations of aftershocks during this period, and the color of the dots represents the number of aftershocks within 0.25° of the surrounding area. Green circles show the four aftershock concentration zones. Black contours represent the sub-daily coseismic slip distribution, and the alternating red and light gray contours represent the cumulative afterslip distribution 36 h after the earthquake

aftershocks are clustered in two areas in the northern part of the fault, both north and south of the aftershock concentration. After 2–8 h, the number of aftershocks shift southward and concentrate in the edges of the two afterslip concentration zones. The aftershock migration pattern is consistent with the spatial expansion of the afterslip. The number of aftershocks decreases between 8–12 h, with most clusters located around the 0.2 m contour of the afterslip. During the 12–18 h period, there is a spatial merging of afterslip concentrations in the central and southern parts of the fault. This coincides with the location of aftershock swarms, which is consistent with the phenomenon observed in the 2015 Illapel Mw8.3 earthquake (Liu et al., 2022). In the 18–36-h period, the spatial variability of the aftershocks is smaller and mostly located in the boundaries of the afterslip. The aftershocks in the southern cluster vary southwards along the afterslip boundary and are in the shallow boundary of the afterslip zone. This is particularly noticeable during the 24–36 h period, when the aftershocks occur almost

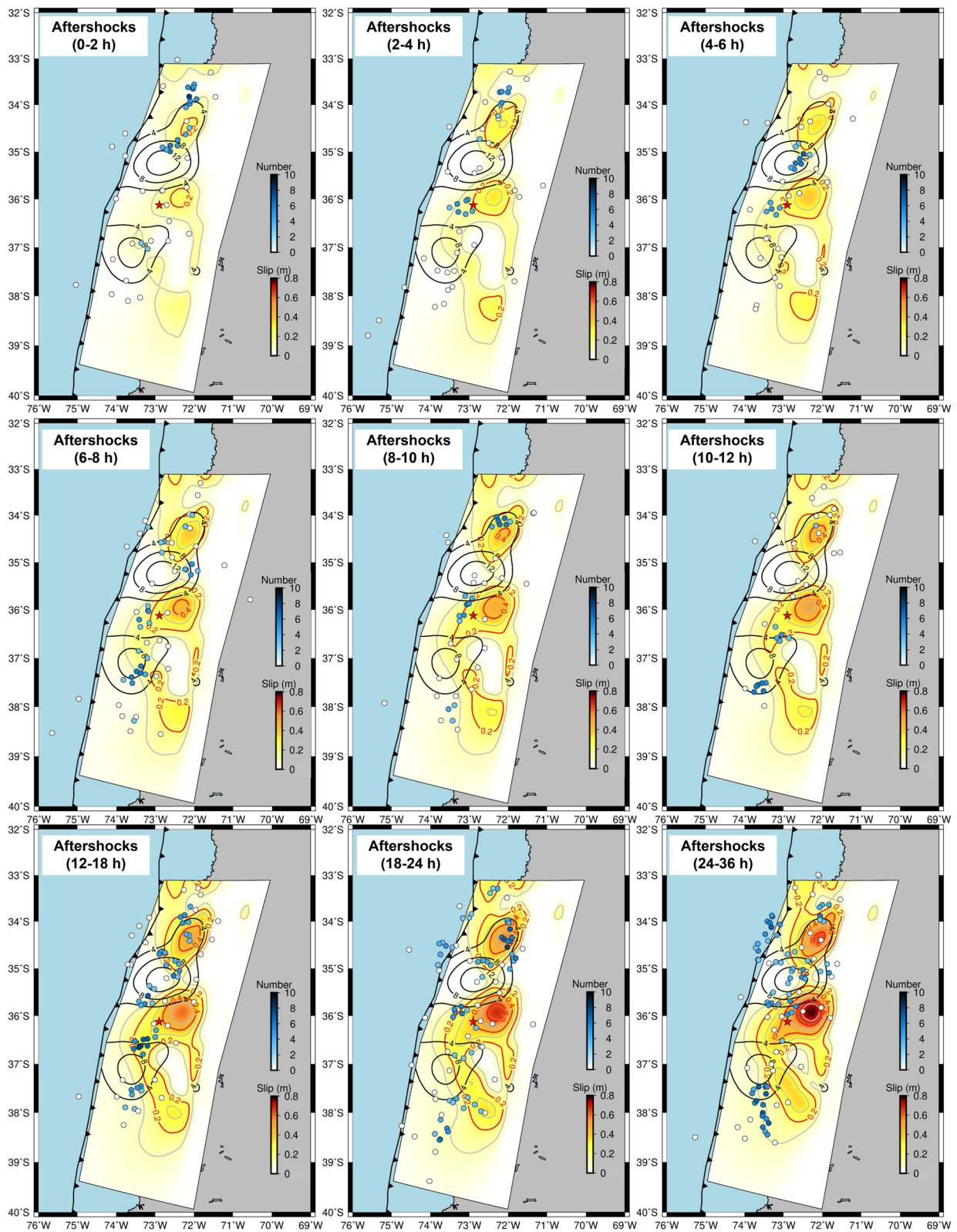


Fig. 10 Evolution of aftershock and afterslip during the first 36 h after the earthquake. The color of the dots indicates the number of surrounding aftershocks. The black, red, and gray contours are same as Fig. 9

exclusively along the afterslip 0.1 m contour, with a nearly identical spatial distribution.

Generally, the locations of aftershocks have a close correlation with the temporal-spatial evolution of the afterslip. Spatially, the aftershocks were predominantly observed in the boundary of the afterslip zone, rather than the maximum-slip zone, and their locations align with the gradual expansion trend of the afterslip zone. From a temporal perspective, during the initial 10 h after the event aftershocks are primarily concentrated around the shallow boundary zone of the afterslip zone in the central and northern areas. As time progresses and the afterslip begins to expand, the distribution of aftershocks becomes more dispersed, gradually progressing towards the shallow and southern regions. In the Maule earthquake, the very early aftershocks and afterslip are correlated in the spatial and temporal evolution, and the correlation with the zones of coseismic slip is weak. Aftershocks generally occur within the afterslip zone, and the gradual progression of afterslip towards the shallow and southern regions of the fault plane over time affects aftershock events. We suggest that afterslip may be a crucial factor in triggering aftershocks, consistent with the previously discovered correlation between early evolution (Liu et al., 2022; Miliner et al., 2020; Tsang et al., 2019) and long-term post-seismic activities (Agurto et al., 2012; Lange et al., 2012).

Conclusion

Coseismic and postseismic deformations resulting from the 2010 Maule earthquake were obtained with kinematic GPS. Our findings indicate that daily GPS solutions overestimate coseismic deformations by almost 10%. In addition, the surface deformation during the initial phase of the postseismic activity is significant, and afterslip is the main mechanism responsible for the rapid early surface deformation. There is a certain correlation between the spatial and temporal evolution processes of aftershocks and afterslip, with most aftershocks taking place in the boundary of the afterslip zone.

Earthquakes exhibit distinct characteristics in surface deformation during their origin, occurrence, and adjustment, but the transition between these phases is entirely continuous. At present, GNSS may be the sole space-based geodetic method that is suitable for monitoring such ongoing deformations. Continuous improvements in the spatial resolution of GNSS ground-based observations can be achieved by upgrading ground GNSS networks. Hence, further study of very early postseismic deformation using sub-daily or high-rate GNSS solutions can better observe the continuous deformations (including seismic waveforms, coseismic permanent deformation, and early post-seismic deformation) of the surface near the faults, which

is of great importance for completely capturing postseismic deformations, as well as for better understanding the activity characteristics and tectonic mechanisms of faults in the postseismic phase, both initially and overall.

Abbreviations

CODE	Center for orbit determination in Europe
CSN	Chilean seismological center
GIM	Global ionosphere map
GNSS	Global navigation satellite system
GPS	Global positioning system
IGS	International GNSS service
InSAR	Interferometric synthetic aperture radar
PDOP	Position dilution of precision
USGS	United States geological survey
UTC	Coordinated universal time

Supplementary Information

The online version contains supplementary material available at <https://doi.org/10.1186/s43020-024-00145-6>.

Supplementary file 1.

Acknowledgements

We have benefited from fruitful discussions with Dr. Jiangtao Li and Dr. Guangcai Li.

Author contributions

J.G. led the project and proposed the idea; K.L. and Y.W. carried out the experiments; K.L. and Z.L. drafted the manuscript; J.Z. processed the kinematic data; C.X. controlled the quality of this study; all reviewed and approved the manuscript.

Funding

This work is funded by the National Natural Science Foundation of China (42025401 and 42374003), and the Hubei LuoJia Laboratory (No. 220100021).

Availability of data and materials

The GNSS data of the 2010 Maule earthquake are provided by CSN at the Universidad de Chile (<http://gps.csn.uchile.cl/data/>). Data from USGS are available at <https://earthquake.usgs.gov/earthquakes/eventpage>.

Declarations

Competing interests

Jianghui Geng is an editorial board member for *Satellite Navigation* and was not involved in the editorial review or decision to publish this article. All authors declare that they have no competing interests.

Received: 30 October 2023 Accepted: 23 May 2024

Published: 29 July 2024

References

- Aguirre, L., Bataille, K., Novoa, C., Pena, C., & Vera, F. (2019). Kinematics of subduction processes during the earthquake cycle in central Chile. *Seismological Research Letters*, 90(5), 1779–1791.
- Agurto, H., Rietbrock, A., Ryder, I., & Miller, M. (2012). Seismic-afterslip characterization of the 2010 Mw 8.8 Maule Chile earthquake based on moment tensor inversion. *Geophysical Research Letters*, 39(20), 1.
- Altamimi, Z. X., Collilieux, J., Legrand, B., Garayt, and C. Boucher. (2007). ITRF2005: A new release of the International Terrestrial Reference Frame based on time series of station positions and earth orientation parameters, *J Geophys Res-Sol EA*, 112(B9)

- Banville, S., Sieradzki, R., Hoque, M., Wezka, K., & Hadas, T. (2017). On the estimation of higher-order ionospheric effects in precise point positioning. *GPS Solutions*, 21(4), 12.
- Bedford, J., Moreno, M., Baez, J. C., Lange, D., Tilmann, F., Rosenau, M., Heidbach, O., Oncken, O., Bartsch, M., Rietbrock, A., Tassara, A., Bevis, M., & Vigny, C. (2013). A high-resolution, time-variable afterslip model for the 2010 Maule Mw=8.8 Chile Megathrust Earthquake. *Earth Planet SC Lett*, 383, 26–36.
- Bedford, J., Moreno, M., Li, S. Y., Oncken, O., Baez, J. C., Bevis, M., Heidbach, O., & Lange, D. (2016). Separating rapid relocking, afterslip, and viscoelastic relaxation: An application of the postseismic straightening method to the Maule 2010 cGPS. *Journal of Geophysical Research Solid Earth*, 121(10), 7618–7638.
- Bilich, A., Cassidy, J. F., & Larson, K. M. (2008). GPS seismology: Application to the 2002 M-w 7.9 Denali fault earthquake. *Bulletin of the Seismological Society of America*, 98(2), 593–606.
- Bock, Y., & Melgar, D. (2016). Physical applications of GPS geodesy: A review. *Reports on Progress in Physics*, 79(10), 106801.
- Burgmann, R., & Dresen, G. (2008). Rheology of the lower crust and upper mantle: Evidence from rock mechanics, geodesy, and field observations. *Annu Rev Earth PL SC*, 36, 37.
- Delouis, B., Nocquet, J. M., & Vallée, M. (2010). Slip distribution of the February 27, 2010 Mw= 8.8 Maule earthquake, central Chile, from static and high-rate GPS, InSAR, and broadband teleseismic data. *Geophysical Research Letters*, 37(17), 1.
- Freed, A. M. (2005). Earthquake triggering by static, dynamic, and postseismic stress transfer. *Annu Rev Earth PL SC*, 33, 335–367.
- Geng, J., Chen, X., Pan, Y., Mao, S., Li, C., Zhou, J., & Zhang, K. (2019). PRIDE PPP-AR: an open-source software for GPS PPP ambiguity resolution. *GPS Solutions*, 23, 1.
- Geng, J. H., Pan, Y. X., Li, X. T., Guo, J., Liu, J. A., Chen, X. C., & Zhang, Y. (2018). Noise characteristics of high-rate multi-GNSS for subdaily crustal deformation monitoring. *J Geophys Res-Sol EA*, 123(2), 1987–2002.
- Genrich, J. F., & Bock, Y. (1992). Rapid resolution of crustal motion at short ranges with the global positioning system. *Journal of Geophysical Research: Solid Earth*, 97(B3), 3261–3269.
- Golriz, D., Bock, Y., & Xu, X. (2021). Defining the coseismic phase of the crustal deformation cycle with seismogeodesy. *Journal of Geophysical Research: Solid Earth*, 126(10), 2021022002.
- Hayes, G. P., Moore, G. L., Portner, D. E., Hearne, M., Flamme, H., Furtney, M., & Smoczyk, G. M. (2018). Slab2, a comprehensive subduction zone geometry model. *Science*, 362(6410), 58–61.
- Jonsson, S., Segall, P., Pedersen, R., & Björnsson, G. (2003). Post-earthquake ground movements correlated to pore-pressure transients. *Nature*, 424(6945), 179–183.
- Klein, E., Fleitout, L., Vigny, C., & Garaud, J. D. (2016). Afterslip and viscoelastic relaxation model inferred from the large-scale post-seismic deformation following the 2010 M w 8.8 Maule earthquake (Chile). *Geophysical Journal International*, 205(3), 1455–1472.
- Langbein, J., Murray, J. R., & Snyder, H. A. (2006). Coseismic and initial postseismic deformation from the 2004 Parkfield California, earthquake, observed by global positioning system, electronic distance meter, creepmeters, and borehole strainmeters. *Bulletin of the Seismological Society of America*, 96S(4B), S304–S320.
- Lange, D., Tilmann, F., Barrientos, S. E., Contreras-Reyes, E., Methe, P., Moreno, M., Heit, B., Agurto, H., Bernard, P., Vilotte, J. P., & Beck, S. (2012). Aftershock seismicity of the 27 February 2010 Mw 8.8 Maule earthquake rupture zone. *Earth Planet SC Lett*, 317, 413–425.
- Larson, K. M. (2009). GPS seismology. *Journal of Geodesy*, 83(3–4), 227–233.
- Lin, Y., Sladen, A., Ortega-Culaciati, F., Simons, M., Avouac, J. P., Fielding, E. J., Brooks, B. A., Bevis, M., Genrich, J., Rietbrock, A., Vigny, C., Smalley, R., & Socquet, A. (2013). Coseismic and postseismic slip associated with the 2010 Maule earthquake, Chile: Characterizing the Arauco Peninsula barrier effect. *JGR Solid Earth*, 118(6), 3142–3159.
- Liu, K., Geng, J., Wen, Y., Ortega-Culaciati, F., & Comte, D. (2022). Very early postseismic deformation following the 2015 Mw 8.3 Illapel earthquake, Chile revealed from kinematic GPS. *Geophysical Research Letters*, 49(11), 2022098526.
- McCormack, K., Hesse, M. A., Dixon, T., & Malservisi, R. (2020). Modeling the contribution of Poroelastic deformation to Postseismic geodetic signals. *Geophysical Research Letters*, 47(8), 10.
- Milliner, C., Bürgmann, R., Inbal, A., Wang, T., & Liang, C. (2020). Resolving the kinematics and moment release of early afterslip within the first hours following the 2016 Mw 7.1 Kumamoto earthquake: Implications for the shallow slip deficit and frictional behavior of aseismic creep. *Journal of Geophysical Research: Solid Earth*, 125(9), 2019018928.
- Okada, Y. (1992). Internal deformation due to shear and tensile fault in a half space. *B Seismol SOC AM*, 82(2), 1018–1040.
- Peltzer, G., Rosen, P., Rogez, F., & Hudnut, K. (1996). Post seismic rebound in fault step-overs caused by pore fluid flow. *Science*, 273(5279), 3.
- Pena, C., Heidbach, O., Moreno, M., Bedford, J., Ziegler, M., Tassara, A., & Oncken, O. (2019). Role of lower crust in the Postseismic deformation of the 2010 Maule earthquake: Insights from a model with power-law rheology. *Pure and Applied Geophysics*, 176(9), 3913–3928.
- Peña, C., Metzger, S., Heidbach, O., Bedford, J., Bookhagen, B., Moreno, M., Oncken, O., & Cotton, F. (2022). Role of Poroelasticity During the Early Postseismic Deformation of the 2010 Maule Megathrust Earthquake. *Geophysical Research Letters*, 49(9), 2022098144.
- Perfettini, H., & Ampuero, J. P. (2008). Dynamics of a velocity strengthening fault region: Implications for slow earthquakes and postseismic slip. *Journal of Geophysical Research Solid Earth*, 113(9), 1.
- Perfettini, H., & Avouac, J. P. (2004). Postseismic relaxation driven by brittle creep: A possible mechanism to reconcile geodetic measurements and the decay rate of aftershocks, application to the Chi-Chi earthquake Taiwan. *Journal of Geophysical Research: Solid Earth*, 109(2), 1.
- Rietbrock, A., Ryder, I., Hayes, G., Haberland, C., Comte, D., Roecker, S., & Lyon-Caen, H. (2012). Aftershock seismicity of the 2010 Maule Mw= 8.8, Chile, earthquake: Correlation between co-seismic slip models and aftershock distribution? *Geophysical Research Letters*, 39(8), 1.
- Ruegg, J. C., Rudloff, A., Vigny, C., Madariaga, R., de Chabaliér, J. B., Campos, J., Kausel, E., Barrientos, S., & Dimitrov, D. (2009). Interseismic strain accumulation measured by GPS in the seismic gap between Constitución and Concepción in Chile. *Physics of the Earth and Planetary Interiors*, 175(1–2), 78–85.
- Tong, X., Sandwell, D., Luttrell, K., Brooks, B., Bevis, M., Shimada, M., Foster, J., Smalley, R., Jr., Parra, H., Báez Soto, J. C., & Blanco, M. (2010). The 2010 Maule, Chile earthquake: Downdip rupture limit revealed by space geodesy. *Geophysical Research Letters*, 37(24), 1.
- Tsang, L. L., Vergnolle, M., Twardzik, C., Sladen, A., Nocquet, J. M., Rolandone, F., Agurto-Detzel, H., Cavalié, O., Jarrin, P., & Mothes, P. (2019). Imaging rapid early afterslip of the 2016 Pedernales earthquake, Ecuador. *Earth and Planetary Science Letters*, 15(524), 115724.
- Twardzik, C., Vergnolle, M., Sladen, A., & Avallone, A. (2019). Unravelling the contribution of early postseismic deformation using sub-daily GNSS positioning. *Scientific Reports*, 9(1), 1775.
- Vigny, C., Socquet, A., Peyrat, S. et al. (2011). The 2010 M-w 8.8 Maule megathrust earthquake of central Chile Monitored by GPS. *Science*, 332(6036), 1417–1421.
- Wang, K., Hu, Y., & He, J. (2012). Deformation cycles of subduction earthquakes in a viscoelastic Earth. *Nature*, 484(7394), 6.
- Wang, R., Schurr, B., Milkereit, C., Shao, Z., & Jin, M. (2011). An improved automatic scheme for empirical baseline correction of digital strong-motion records. *Bulletin of the Seismological Society of America*, 101(5), 2029–2044.
- Weiss, J. R., Qiu, Q., Barbot, S., Wright, T. J., Foster, J. H., Saunders, A., Brooks, B. A., Bevis, M., Kendrick, E., Ericksen, T. L., & Avery, J. (2019). Illuminating subduction zone rheological properties in the wake of a giant earthquake. *Science Advances*, 5(12), 6720.
- Wright, T. J., Parsons, B., England, P. C., & Fielding, E. J. (2004). InSAR observations of low slip rates on the major faults of western Tibet. *Science*, 305(5681), 4.

Publisher's Note

Springer Nature remains neutral with regard to jurisdictional claims in published maps and institutional affiliations.